PERGAMON

International Journal of Heat and Mass Transfer 43 (2000) 113–126

International Journal of HEAT and MASS TRANSFER

www.elsevier.com/locate/ijhmt

Constrained optimal duct shapes for conjugate laminar forced convection

T.S. Fisher*, K.E. Torrance

Sibley School of Mechanical and Aerospace Engineering, Cornell University, Ithaca, NY 14853, USA

Received 20 August 1998; received in revised form 26 March 1999

Abstract

The complex variable boundary element method (CVBEM) is used to analyze conjugate heat transfer in solids with cooling passages of general, convex cross section. The method is well-suited to duct cross sections with high curvature and high aspect ratios because the whole-domain boundary integrals are path independent and analytic. The effects of channel boundary curvature on overall heat transfer are quantified for the first time. Shape-constrained optimal solutions involving fixed pressure drop and fixed pump work are presented. Increased channel boundary curvature is shown to decrease the optimal distance between parallel channels by increasing fin efficiency.

1. Introduction

The cooling of high-power electronic devices requires renewed attention as power dissipation from electronic components continues to increase. Reflecting the trends in electrical microcircuits, the size of cooling systems must decrease while power dissipation increases. Although many different techniques could potentially provide adequate cooling, small-scale channels embedded in a solid substrate offer particular promise due to their small sizes and high rates of heat transfer. The present paper provides some constrained optimal solutions of duct shape for conjugate laminar forced convection, using a versatile, but accurate, complex-variable form of the boundary element method.

Much prior work has focused on the prediction and measurement of heat transfer in small-scale channels (often called microchannels). Early work by Tuckerman and Pease [1–3] established a general theory and foundational experiments for microchannel cooling. Since their work, many others have studied such systems analytically, experimentally, and computationally. Philips [4] provided a thorough review of the literature for years prior to 1990. Since then, many researchers have studied different aspects of microchannel cooling. The most relevant to the present study is the work by Bau and co-workers [5,6] in which conjugate heat transfer is modeled computationally.

The present work addresses the analysis of small-scale channels with general, curved boundaries. Such channels are important for a variety of reasons. First, the fabrication of such channels often does not produce exact, rectangular cross sections, as evidenced for example, by the substrate cross sections shown by Tuckerman [3] and Hoopman [7]. Second, the sharp corners of rectangular channels inhibit local heat transfer by restricting fluid flow. Third, a curved boundary can significantly increase the surface efficiencies of high aspect-ratio fins. Channels with curved boundaries

* Corresponding author. Vanderbilt University, Department of Mechanical Engineering, Box 1592—Station B, Nashville, TN 37235. Tel.: +1-615-322-2956; fax: +1-615-343-6687.

E-mail address: tim.fisher@vanderbilt.edu (T.S. Fisher)

0017-9310/00/$ - see front matter
PII: S0017-9310(99)00115-5

Nomenclature

a, b	channel half-width and half-height, see Eq. (21) (m)
a_k, b_k, c_k	coefficients in the quadratic spline interpolation
∂B	domain boundary descriptor
c_1, c_2	constants in Poisson equations, see Eqs. (4) and (5)
$\Im$	imaginary part
J_k	Jacobian for element k
k_f, k_s	fluid and solid thermal conductivities (W/mK)
$K(\infty)$	Hagenbach factor, see Eq. (28)
L	channel length (m)
n	normal boundary coordinate
P	fluid pressure (Pa)
q''	heat flow per unit area (W/m^2)
r_x	nondimensional cross-sectional thermal resistance, see Eq. (39)
$\Re$	real part
$\mathscr{R}''$	total thermal resistance per unit surface area (K m^2/W), see Eq. (18)
$\mathscr{R}''_x$	cross-sectional thermal resistance per unit surface area (K m^2/W), see Eq. (38)
$\mathscr{R}''_{bulk}$	bulk thermal resistance per unit surface area (K m^2/W), see Eq. (41)
s	tangential boundary coordinate
t	complex field variable
t_c	conduction thickness, see Fig. 1 (m)
t_f	fin half-thickness, see Fig. 1 (m)
T_f, T_s	fluid and solid temperatures (K)
T_B	bulk (mixed-mean) fluid temperature (K)
u, v	real and imaginary parts of the function w
w	complex analytic function
W	fluid velocity (m/s)
$\dot{W}'$	pump work rate per unit transverse width (W/m)
X, Y, Z	horizontal, vertical, and axial coordinates (m)
z	complex source point.

Greek symbols

α	boundary surface angle
α_f	fluid thermal diffusivity (m^2/s)
α^*	channel aspect ratio, $2a/b$
ϵ	curvature parameter, see Eq. (21)
$\vartheta(z)$	analytic function, see Eq. (6)
μ	fluid dynamic viscosity (N s/m^2)
ρ	fluid density (kg/m^3)
$\phi(z)$	analytic function, see Eq. (6)
$\psi(z)$	analytic function, see Eq. (8).

have not been previously studied because they are not readily amenable to the straightforward fin/resistance networks employed by many researchers in the area [8,9], or to traditional computational methods [5,6] such as the finite element and finite difference methods.

The present work utilizes the complex variable boundary element method (CVBEM) to solve for heat transfer in ducts with curved cross-sectional boundaries. The CVBEM is particularly well suited to such problems because discretized whole-domain integrals are path independent and evaluated analytically. Thus, the formulation is highly accurate, and specialized treatment of boundary curvature is minimal. Further, the method provides an inherent means of error estimation for boundary grid refinement.

For fully developed flow with uniform axial heating, the governing momentum and energy equations can be combined, with appropriate assumptions, to form a single biharmonic equation. The resulting equation is analogous to that found in the theory of thin-plate elasticity [10]. Thus, classical work on plate elasticity [11] for typical boundary shapes is applicable to the present theory. More recently, Gu and Huang [12] employed a variation of the complex variable boundary element method to study plate elasticity. Their development began with Vekua's formula [13] to generate boundary integral equations. In contrast to Cauchy's integral formula, Vekua's formula integrates with respect to the real-valued boundary arc length. The resulting integrals are more difficult to evaluate on curved boundaries than are integrals based on Cauchy's integral equation. Barbuto and Cotta [14] used a real-variable integral transform method [15] to model the flow fields in ducts of irregular cross section. The utility of the integral transform method depends strongly on the ability to parameterize the boundary shape.

Boundary methods can be formulated using complex variables for two-dimensional problems. Early work on the complex variable boundary element method was performed by Hromadka and Guymon [16] and Brevig et al. [17]. A general description of the CVBEM has been provided by Hromadka [18] and Hromadka and Lai [19]. Since its introduction, the CVBEM has been applied to potential problems [20–23], plane and plate elasticity [12,24], and grid generation [25–28]. The number of applications for the CVBEM will likely grow in the future.

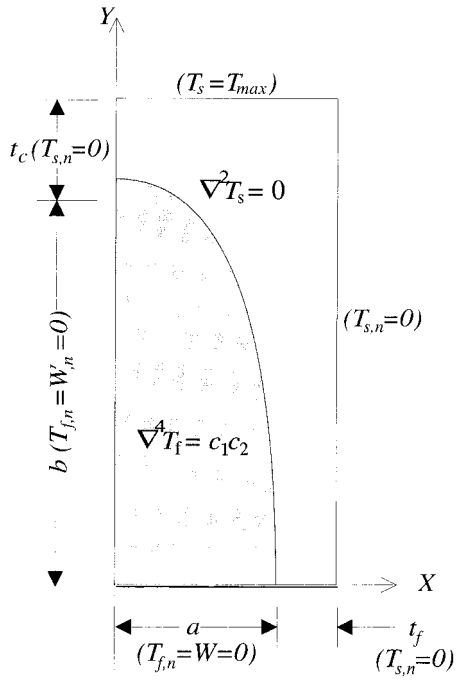

Fig. 1. Computational domain for conjugate heat transfer. Boundary conditions are shown in parentheses. Due to symmetry, the computational domain is one-half of the physical domain.

The present work considers the effects of channel shape on conjugate heat transfer and employs the CVBEM to obtain numerical solutions. Channel shape (i.e., curvature) can significantly affect the Nusselt number, friction factor, and entrance-region pressure drop. All the foregoing parameters influence heat transfer performance under typical flow constraints such as fixed pressure drop or pump work. Further, the present work includes an accurate prediction of conjugate heat transfer in fin-like structures. The computational modeling eliminates many of the approximations, such as a uniform heat transfer coefficient and one-dimensional heat conduction, used by prior workers [8,9]. The objectives here are to introduce a new computational method for the modeling of conjugate heat transfer in solids with curved-boundary cooling channels and to quantify the effects of channel curvature on the thermal and hydrodynamic performance of the systems.

2. Mathematical formulation

Small-scale channels can be fabricated by a variety of techniques [4,7]. We assume here that the channels are straight and of uniform cross section. A sketch of a solid substrate and cooling channel is shown in Fig. 1.

The upper boundary is assumed to be isothermal, with heat flowing from that boundary to the cooling channel by conduction. The vertical boundaries are symmetry planes (horizontally repeating). The lower boundary is rigid and adiabatic. Due to symmetry about $X = 0$ in Fig. 1, only half a channel is modeled. The height and half-width of the channels are b and a, respectively. The channel wall's half-thickness at the bottom of the channel is denoted by t_f, and the conduction thickness between the top of the substrate and the top of the channel is represented by t_c. The length L of the channel is not shown in the figure and is assumed to be 5 cm unless otherwise stated. A finite channel length L is required to scale the exit temperature.

In developing a mathematical formulation, several assumptions are made:

1. The flow is laminar and fully developed thermally and hydrodynamically.
2. All material properties are constant.
3. Axial conduction in both solid and fluid domains is negligible.
4. The bottom of the system ($Y = 0$ in Fig. 1) is capped by a thermally insulating material, resulting in a normal heat flux of zero.

The first assumption reflects the fact that the hydraulic diameters ($D_h \equiv 4 \times$ area/perimeter) of interest here are of order 10^2 to 10^3 μm, and the associated Reynolds numbers are of order 10^2 to 10^3. Consequently, the laminar flow assumption is well justified, and the hydrodynamic and thermal entrance lengths for air and water are typically $L_e \sim \mathcal{O}(10^{-2}$ m) or less. Thus, the fully developed assumption is appropriate. Further, hydrodynamic entrance effects are estimated from the fully developed solution by calculating the Hagenbach factor for the inlet pressure drop.

The second assumption above provides generality, and allows us to present results in terms of thermal resistances, which otherwise become case-specific. Regarding the third assumption, Weisberg et al. [5] estimated axial conduction to be less than 1% of the cross-sectional heat flow. The fourth assumption reflects the reality of small-scale channel fabrication.

Subsequent sections describe the governing equations and the mathematical outline for the present complex variable boundary element method. Further details are available in Fisher [29] or, for the non-conjugate duct problem, in Fisher and Torrance [30]. Readers wishing to directly see results should go to Sections 2.4, 2.6, 2.7 and 3.

2.1. Governing equations

With the foregoing assumptions, the problem reduces to two dimensions. The conjugate equations for velocity and temperature become

$$\nabla^2 W = c_1 \tag{1}$$

$$\nabla^4 T_f = c_1 c_2 \tag{2}$$

$$\nabla^2 T_s = 0 \tag{3}$$

where the Laplace and biharmonic operators involve only the X–Y coordinates in the plane of Fig. 1. The subscripts 'f' and 's' denote the fluid and solid regions, and the coefficients c_1 and c_2 are given by

$$c_1 = \frac{1}{\mu}\frac{dP}{dZ} \tag{4}$$

$$c_2 = \frac{1}{\alpha_f}\frac{\partial T_f}{\partial Z}. \tag{5}$$

Z is the axial coordinate perpendicular to the plane of Fig. 1. As shown by Fisher and Torrance [30], the solution for the temperature of the fluid is divisible into homogeneous and particular parts, resulting in a temperature field described by

$$T_f = \Re\{\vartheta(z) + \bar{z}\,\phi(z)\} + \frac{c_1 c_2}{64} z^2 \bar{z}^2 \tag{6}$$

where z is the complex variable $z = X + iY$ and $\bar{z}$ is its complex conjugate. $\vartheta(z)$ and $\phi(z)$ are complex analytic functions, and the second term on the right side of Eq. (6) is a particular solution to Eq. (2). The fluid velocity W is a function of $\phi(z)$ as

$$W = \frac{4}{c_2}\Re\{\phi'(z)\} + \frac{c_1}{4} z\bar{z} \tag{7}$$

where the prime symbol denotes the complex derivative (d/dz). The solid temperature field is governed by Laplace's equation, and therefore admits a solution of the form

$$T_s = \Re\{\psi(z)\} \tag{8}$$

where ψ is a complex, analytic function. The analytic functions ϑ, ϕ, and ψ constitute the set of unknowns in the present problem.

2.2. Boundary integral equations

The previous section showed that the solutions for fluid velocity, fluid temperature, and solid temperature are expressible in terms of the analytic functions ϕ, ϑ, and ψ. The value of a generic, analytic function $w = u + iv$ can be represented through Plemelj's formula [31] as

$$\frac{\alpha}{2\pi} w(z) = \frac{1}{2\pi i} \int\!\!\!\!\!\!\diagup_{\partial B} \frac{w(t)}{t - z}\, dt \tag{9}$$

where z is a boundary point, α represents the included angle of the boundary's surface (e.g., $\alpha = \pi/2$ if z lies on a corner of a square domain), and $\int\!\!\!\!\!\!\diagup$ represents the Cauchy principal value integral [32]. Eq. (9) expresses the value of the analytic function w at a boundary point z in terms of the function's value at other points on the boundary. Note that the integrand, $w(t)/(t-z)$, becomes singular as the field point t approaches the source point z. The singularity can be integrated exactly.

The boundaries of the fluid and solid domains are subdivided into N_f and N_s elements, respectively. For either the solid or fluid domain, the discrete form of Eq. (9) is

$$\frac{\alpha}{2\pi} w_i = \frac{1}{2\pi i} \sum_{k=1}^{N} \int\!\!\!\!\!\!\diagup_{\partial B_k} \frac{w_k(t)}{t - z_i}\, dt \tag{10}$$

where w_i is the value of the analytic function at the boundary points z_i, and $w_k(t)$ is an interpolation function for w on a boundary segment ∂B_k. Quadratic spline interpolation is employed to represent the analytic functions on each element in order to maintain element-to-element continuity of the function ϕ, which partially describes the temperature field, as well as its first complex derivative ϕ', which represents the velocity field. The interpolation function takes the general form

$$w_k(t) = a_k + b_k(t - z_k) + c_k(t - z_k)^2 \tag{11}$$

where a_k, b_k and c_k are complex constants. The integrand in Eq. (10) becomes singular for $k = i$, and the resulting integral is evaluated exactly from its Cauchy principal value.

In fact, all integrals in Eq. (10) can be evaluated analytically when combined with the interpolation function in Eq. (11). The final form of the integrated boundary integral equation is [29,30]

$$w_i = \frac{w_i}{2\pi i}\ln\frac{(z_{i+1}-z_i)}{(z_{i-1}-z_i)} + \frac{1}{2\pi i}\sum_{k\neq i,\ i-1}[w_k + w_k'(z_i-z_k) + c_k(z_i-z_k)^2]\ln\frac{(z_{k+1}-z_i)}{(z_k-z_i)} + \frac{1}{2\pi i}\sum_{k=1}^{N}[w_k' + 2c_k(z_i-z_k)](z_{k+1}-z_k) + \frac{1}{2}c_k[(z_{k+1}-z_i)^2-(z_k-z_i)^2]. \quad (12)$$

Again, note the absence of numerical quadrature. Further, each integral is path independent. Thus, each integral relies only on knowledge of a boundary element's endpoints (i.e., nodes) and not on the shape of the path between endpoints. This path independence makes the present formulation well-suited to the modeling of domains with curved boundaries.

The integrated form of the boundary integral equation in Eq. (12) includes three vectors of unknowns, w_k, w_k' and c_k. The latter vectors are linearly related to the first by quadratic spline relations. Thus, a system of equations of the form $A_{ik}w_k = 0$ can be readily derived from Eq. (12).

Depending on the type of boundary condition at a given node or element, either the real or imaginary part of the complex boundary integral equation is selected as the real-valued boundary integral equation. The selections of real-valued boundary integral equations are governed by the temperature and velocity boundary conditions, as dictated by the 'implicit' formulation of Hromadka and Lai [19]. This section process produces N_f equations each for ϕ (or velocity) and ϑ (or fluid temperature), and N_s equations for ψ (or solid temperature). The discarded boundary integral equations are used to estimate errors and refine the mesh as described by Fisher and Torrance [30]. This inherent ability to estimate errors is a strong advantage of the CVBEM as compared to other numerical methods. Boundary condition equations then complete the set of $2N_f$ equations for velocity (or ϕ) and $2(N_f + N_s)$ equations for the coupled temperature fields (or ϑ and ψ).

2.3. Boundary conditions

The boundary conditions for the present problem are shown in Fig. 1. The subscripts ',n' denote normal derivatives at the boundary. The boundary conditions on fluid velocity are similar to those described by Fisher and Torrance [30] and take the form

Dirichlet: $$\frac{4}{c_2}\Re\{\phi_k'\} = \tilde{W}_k - \frac{c_1}{4}z_k\bar{z}_k \quad (13)$$

Neumann:

$$\frac{4}{c_2}\Im\{\phi_{k+1}'-\phi_k'\} = \int_{\partial B_k}\left[\tilde{W}_{,\,n} - \frac{c_1}{2}\Re\{e^{i\theta_n}\bar{z}\}\right]ds \quad (14)$$

where the tilde ($\tilde{}$) denotes an imposed boundary condition value. Note that Neumann conditions are integrated [as in Eq. (14)] into 'stream function' conditions, as dictated by the complex variable formulation. The Neumann conditions on fluid temperature along straight segments ($Y = 0$ and $X = 0$) of the boundary can be expressed as

$$\Im\{\vartheta_{k+1}-\vartheta_k\} = \int_{\partial B_k}\left[\tilde{T}_{,\,n} - \frac{\partial}{\partial n}\left(\frac{c_1c_2}{64}z^2\bar{z}^2 + \Re\{\bar{z}\phi(z)\}\right)\right]ds. \quad (15)$$

The temperature boundary conditions at the fluid/solid interface are treated at the end of this subsection.

The boundary conditions on solid temperature are generally simpler than those on fluid variables, due to the fact that the particular solution is zero in the solid domain. The Neumann conditions on the solid-domain boundary elements (along $X = 0$, $X = a + t_f$ and $Y = 0$) take the general form

$$\Im\{\psi_{k+1}-\psi_k\} = \int_{\partial B_k}\tilde{T}_{s,\,n}\,ds \quad (16)$$

while Dirichlet conditions are expressed as

$$\Re\{\psi_k\} = \tilde{T}_s. \quad (17)$$

A Dirichlet condition $\tilde{T}_s = T_{max}$ is imposed on the top surface of the substrate. The condition represents an idealization of a practical system and facilitates the calculation of an area-based thermal resistance

$$\mathscr{R}'' = \frac{T_{max} - T_{inlet}}{\overline{q''}} \quad (18)$$

where T_{inlet} is the inlet fluid temperature and $\overline{q''}$ is the average heat flow per unit area into the top surface of the substrate. The presence of a Dirichlet condition enables a precise calculation of the temperature field. Prior workers [5] have imposed an idealized Neumann condition on the top surface. Such an approach requires special measures to obtain a unique solution for temperature. In the present work, we choose to impose the temperature, while the average heat flux is included in the constant c_2. The difference between the two approaches in terms of thermal resistance is negligible for substrates with high thermal conductivities.

Interfacial boundary conditions along the curved

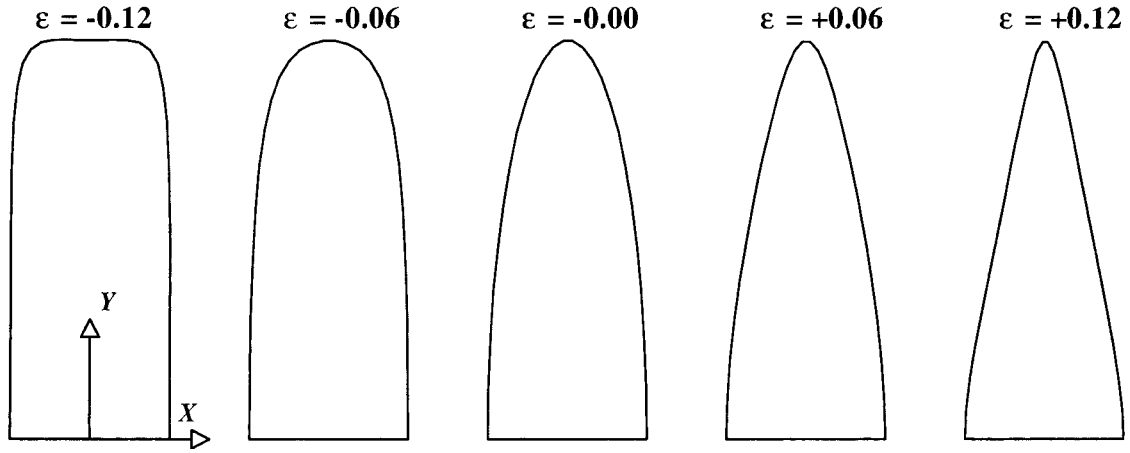

Fig. 2. Parameterized channel boundary shapes with $-0.12 \leq \epsilon \leq 0.12$. Channel half-width $a = 1$. Channel half-height $b = 5$. Channel aspect ratio $\alpha^* = 2a/b = 0.4$.

portion of the boundary are generally more difficult to handle. Temperature and heat flux continuity are imposed on each element of the boundary segment. The temperature condition $T_f = T_s$ at node k becomes

$$\Re\{\vartheta_k\} + \Re\{\bar{z}_k \phi_k\} + \frac{c_1 c_2}{64}(z_k \bar{z}_k)^2 = \Re\{\psi_k\}. \tag{19}$$

For Neumann conditions, the heat flux condition $q''_f = -q''_s$ (with q'' based on the outward normal of each domain) becomes upon integration

$$\frac{k_s}{k_f}\Im\{\psi_{k+1} - \psi_k\} = \Im\{\vartheta_{k+1} - \vartheta_k\} + \int_{\partial B_k} \frac{\partial}{\partial n}\left(\frac{c_1 c_2}{64} z^2 \bar{z}^2 + \Re\{\bar{z}\phi(z)\}\right) \mathrm{d}s. \tag{20}$$

In contrast to the entire-domain boundary integral in Eq. (10), which could be carried out analytically, the boundary-segment integrals arising from Neumann boundary conditions cannot. Therefore, all integrals over each boundary element in Eqs. (14)–(16) and (20) were evaluated by five-point Gaussian quadrature.

2.4. Shape parameterization

The present work utilizes a parameterized boundary shape in order to systematically study the effects of curvature on heat transfer. The constrained parameterized shape allows for rounded semi-rectangles, semi-ellipses, and rounded semi-diamonds. Wei et al. [33] used the same shape function to study the effects of hole shape on the elasticity of plates.

The following equations define the shape of the duct's boundary:

$$x(\varphi) = \frac{a}{1+\epsilon}(\cos\ \varphi + \epsilon\ \cos\ 3\varphi) \tag{21a}$$

$$y(\varphi) = \frac{b}{1+\epsilon}(\sin\ \varphi - \epsilon\ \sin\ 3\varphi) \tag{21b}$$

where a and b control the overall width and height of the duct and $-0.12 \leq \epsilon \leq 0.12$ controls the boundary curvature. The quotient $2a/b \equiv \alpha^*$ defines the channel aspect ratio. The parameter φ spans from 0 to π. Several different shapes for ϵ ranging from -0.12 to 0.12 are shown in Fig. 2. Due to symmetry with respect to the Y-axis, only one half of the domain is modeled computationally.

With the boundary shape defined, the various boundary-condition integrals in Section 2.3 can be evaluated. The integrals take the general form

$$I = \int_{\partial B_k} K(z, \bar{z})\, \mathrm{d}s \tag{22}$$

which, for convenience, is converted to a fixed range of integration to assist in the use of Gauss points:

$$I = \int_{-1}^{1} K[z(\eta), \bar{z}(\eta)] J_k(\eta)\, \mathrm{d}\eta. \tag{23}$$

In Eq. (23), η is a scalar ranging from -1 to 1, and $J_k(\eta)$ is a Jacobian, defined as

$$J_k(\eta) = 0.5[x_{,\varphi}(\eta)^2 + y_{,\varphi}(\eta)^2]^{0.5}(\varphi_{k+1} - \varphi_k). \tag{24}$$

On the duct perimeter,

$$x_{,\varphi}(\eta) = \frac{a}{1+\epsilon}[-\sin\ \varphi(\eta) - 3\epsilon\ \sin\ 3\varphi(\eta)] \tag{25a}$$

$$y_{,\varphi}(\eta) = \frac{b}{1+\epsilon}[\cos\ \varphi(\eta) - 3\epsilon\ \cos\ 3\varphi(\eta)] \tag{25b}$$

and

$$\varphi(\eta) = 0.5\varphi_k(1-\eta) + 0.5\varphi_{k+1}(1+\eta). \tag{26}$$

Boundary integrals along planes of symmetry or other straight boundary segments can be evaluated simply. Eq. (23) still applies, but for straight segments, the Jacobian is

$$J_k = 0.5 \mid z_{k+1} - z_k \mid . \tag{27}$$

Note that the Jacobian for straight segments is independent of the integration variable η.

2.5. Solution procedure

The systems of linear equations are solved by LU decomposition. The computational method described here was programmed in Fortran 77 and executed on a Silicon Graphics workstation, model Indy R5000. The solution sequence is described below:

- formulate the common set of complex boundary integral equations for ϕ and ϑ;
- formulate the set of boundary condition equations for ϕ from the velocity boundary conditions;
- assemble and solve the boundary integral and boundary condition equations for ϕ;
- formulate the set of boundary integral equations for ψ;
- formulate the set of boundary condition equations for ϑ and ψ from the temperature boundary conditions;
- assemble and solve the boundary integral and boundary condition equations for the coupled functions ϑ and ψ;
- transform the three analytic functions ϕ, ϑ and ψ into velocities and temperatures.

2.6. Flow constraints

At the beginning of the analysis, a hydrodynamic constraint is placed on the flow through the system. Two common constraints are fixed total pressure drop (ΔP) and fixed pump work rate per unit transverse (X-coordinate in Fig. 1) width ($\dot{W}'$). Weisberg et al. [5] simplified the implementation of flow constraints by neglecting inlet effects on pressure drop. Here, we incorporate such effects by calculating the Hagenbach factor

$$K(\infty) \equiv \frac{\Delta P_{\mathrm{en}}}{\rho\langle W\rangle^2/2} = \frac{2}{A}\int_B \left[\left(\frac{W}{\langle W\rangle}\right)^3 - \left(\frac{W}{\langle W\rangle}\right)^2\right] \mathrm{d}x\,\mathrm{d}y \tag{28}$$

where ΔP_{en} is the incremental pressure drop due to entrance region effects. This procedure adds some complexity to the problem but improves accuracy.

In order to compute the constrained flow field, the velocity equation is first normalized as

$$\nabla^2 W^* = 1 \tag{29}$$

where $W^* = -\mu W/(\mathrm{d}P/\mathrm{d}Z)$ is a normalized velocity. The normalized Poisson equation is then solved as described above. Note that the normalization has no effect on the homogeneous boundary-condition values on velocity.

Once the normalized velocity field has been solved, an area-averaged, normalized velocity $\langle W^*\rangle$ can be computed. The fixed pressure-drop constraint is represented as

$$\Delta P = -L\frac{\mathrm{d}P}{\mathrm{d}Z} + K(\infty)\frac{\rho\langle W\rangle^2}{2} \tag{30}$$

which can be combined with the normalized velocity equation

$$\frac{\mathrm{d}P}{\mathrm{d}Z} = -\mu\frac{\langle W\rangle}{\langle W^*\rangle} \tag{31}$$

to solve for the actual mean velocity as

$$\langle W\rangle = \frac{\dfrac{-\mu L}{\langle W^*\rangle} + \left[\left(\dfrac{\mu L}{\langle W^*\rangle}\right)^2 + 2\rho\Delta P K(\infty)\right]^{1/2}}{\rho K(\infty)}. \tag{32}$$

Once the actual mean velocity is known, the pressure gradient $\mathrm{d}P/\mathrm{d}Z$ can be calculated from Eq. (31), and the first constant c_1 in the source term of Eq. (2) can be established.

For a constraint on the pump work rate $\dot{W}'$, the procedure for deriving $\mathrm{d}P/\mathrm{d}Z$ and the c_1 is similar to that described above. In this case, the constraining equation can be expressed as

$$\frac{\dot{W}'(a+t_{\mathrm{f}})}{A_{1/2}} = \langle W\rangle\Delta P = \mu L\frac{\langle W\rangle^2}{\langle W^*\rangle} + \frac{1}{2}\rho K(\infty)\langle W\rangle^3 \tag{33}$$

where $A_{1/2}$ is one-half of the channel's cross-sectional area and is evaluated exactly as

$$A_{1/2} = \pi ab\frac{1-3\epsilon^2}{4(1+\epsilon)^2}. \tag{34}$$

The solution for the mean fluid velocity from Eq. (33) is

$$\langle W\rangle = F + \frac{C^2}{9B^2F} - \frac{C}{3B} \tag{35}$$

where

$$B = 0.5\rho K(\infty) \quad C = \frac{\mu L}{\langle W^*\rangle} \quad D = \frac{\dot{W}'(a+t_f)}{A_{1/2}}$$

$$F = \left[\frac{D}{2B} - \frac{C^3}{27B^3} + \frac{\sqrt{3D}}{18B^2}\sqrt{27DB^2 - 4C^3}\right]. \tag{36}$$

Again, once the mean velocity is computed from Eq. (35), the terms dP/dZ and c_1 can be calculated.

For either flow constraint, once the mean velocity is known, the second constant c_2 in the source term of Eq. (2) can be computed from

$$c_2 = \frac{1}{\alpha_f}\frac{dT_B}{dZ} = \frac{\overline{q''}(a+t_f)}{k_f A_{1/2}\langle W\rangle} \tag{37}$$

where T_B is the bulk (or mixed-mean) fluid temperature. Once the constants c_1 and c_2 are known, the solution for temperature in the solid and fluid domains proceeds by computing the analytic functions ϑ and ψ.

2.7. Performance metrics

The primary performance metrics in the present study involve the ratio of temperature rise to areal heat flux and are expressed in the units K/(W/cm^2). The overall thermal resistance $\mathscr{R}''$ was defined in Eq. (18). $\mathscr{R}''$ can be expanded into a cross-sectional component $\mathscr{R}''_x$ and an axial component $\mathscr{R}''_{bulk}$. The cross-sectional component is defined as

$$\mathscr{R}''_x = \frac{T_{max} - T_{B,\,out}}{\overline{q''}} \tag{38}$$

where $T_{B,\,out}$ is the bulk temperature of the fluid at the exit of a channel. Another metric used in the present work is the normalized, cross-sectional resistance, defined as

$$r_x = \frac{k_f}{b}\mathscr{R}''_x. \tag{39}$$

To first order, the cross-sectional thermal resistance depends on geometric variables as

$$\mathscr{R}''_x \sim \frac{a(a+t_f)}{b}. \tag{40}$$

The bulk resistance is expressed as

Table 1
Fluid properties at 300 K

Fluid	μ (N s/m^2)	k_f (W/m K)	ρ (kg/m^3)	c_p (J/kg K)
Water	855×10^{-6}	0.613	997	4179
Air	185×10^{-7}	0.0262	1.16	1007

$$\mathscr{R}''_{bulk} = \frac{T_{B,\,out} - T_{inlet}}{\overline{q''}}. \tag{41}$$

The functional dependence of the bulk resistance depends on the type of flow constraint. For fixed pumping power, the first-order dependence is

$$\mathscr{R}''_{bulk} \sim \sqrt{\frac{L^3(a+t_f)}{a^3 b\dot{W}'}}. \tag{42}$$

For fixed pressure drop, the first-order dependence is

$$\mathscr{R}''_{bulk} \sim \frac{L^2(a+t_f)}{a^3 b\Delta P}. \tag{43}$$

The relations in Eqs. (40), (42) and (43) suggest that the total thermal resistance can be minimized with respect to the channel half-width a. The cross-sectional resistance increases quadratically with a, while the bulk resistance decreases as either a^{-1} (for fixed $\dot{W}'$) or a^{-2} (for fixed ΔP) with increasing channel half-width. Optimization with respect to channel width has been previously considered by several workers [1–4,8,9]. Here, we present some results on optimization with respect to a, but pay more attention to second-order effects, including optimal fin thicknesses t_f and boundary shapes.

3. Results and discussion

The computational method described above can be applied to an extremely broad range of practical systems. We limit the present work to systems involving silicon ($k_s = 149$ W/m K) and nickel ($k_s = 90$ W/m K), and either water or air as the coolant. The constant fluid properties are evaluated at 300 K and are shown in Table 1. The fixed substrate dimensions in the present work are $t_c = 500$ μm, $b = 1000$ μm, and $L = 5$ cm; and the inlet fluid temperature is always taken to be 20°C. The channel half-width a, fin half-thickness t_f and the curvature parameter ϵ are varied to study their effects on thermal performance. Most of the results focus on thermal resistances of the order $\mathscr{R}'' \sim 1$ K/(w/cm^2), which is consistent with the projected requirements of microprocessor cooling systems [34]. The accuracy of the results herein was ensured by

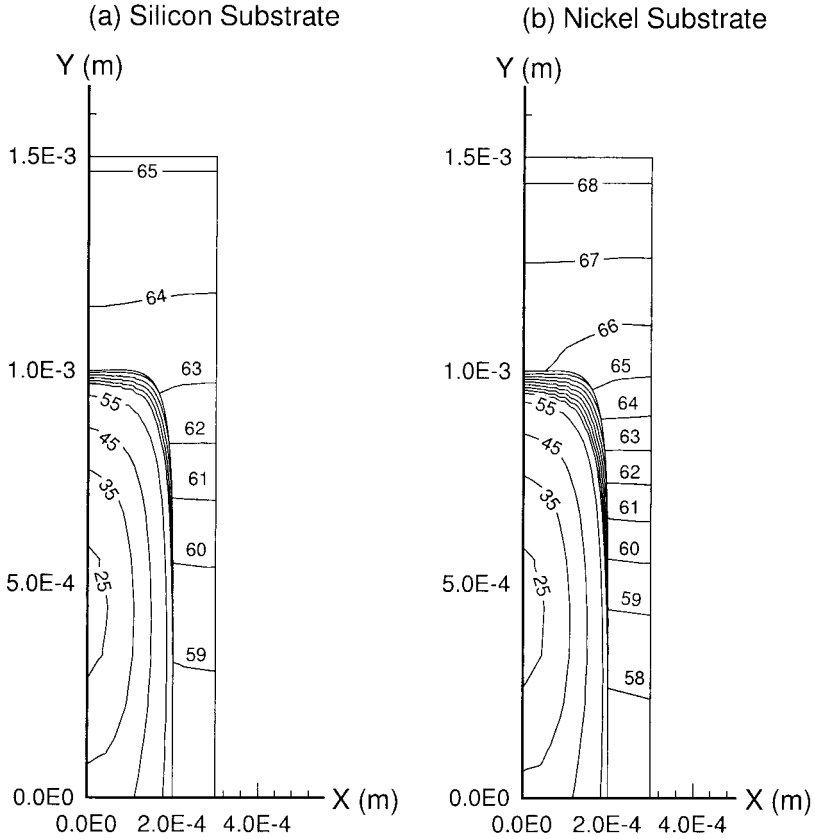

Fig. 3. Exit temperature contours in solid and fluid regions. Fluid = water. Pump work $\dot{W}' = 1$ W/m. Surface heat flux $q'' = 50$ W/cm^2. Channel length $L = 5$ cm. Conduction thickness $t_c = 500$ μm. Channel height $b = 1000$ μm. Channel curvature $\epsilon = -0.12$. Channel half-width $a = 200$ μm. Fin half-thickness $t_f = 100$ μm. (a) Silicon substrate. (b) Nickel substrate.

imposing a maximum internal error estimate (see [30]) of $E = 5 \times 10^{-6}$ for the velocity solution.

3.1. Local temperature fields

Observations of local temperature fields in the solid and fluid regions can provide qualitative insights into the transfer of heat from the top of the substrate, through the fin-like channel walls, and into the convecting fluid. Exit temperature profiles for a silicon and nickel substrate are shown in Fig. 3. For each substrate, the pump work is fixed at $\dot{W}' = 1$ W/m, with a surface heat flux of $q'' = 50$ W/cm^2. The channel and fin half-widths are 200 and 100 μm, respectively, while the curvature parameter is $\epsilon = -0.12$ (corresponding to a rounded rectangle).

Because the pump work and heat flux are fixed, the bulk resistances are the same in parts (a) (silicon) and (b) (nickel) of Fig. 3. Consequently, the bulk fluid temperatures are equal. The heat conduction at the top of the substrates is seen to be nearly one-dimensional. Near the top of the channel in the solid region, the isothermal contour lines become curved, thus illustrating the constriction of heat flow into the fin. The conduction in the fin is nearly one-dimensional, as illustrated by the nearly horizontal isotherms.

The temperature ranges in the different substrates illustrate the effect of solid thermal conductivity on thermal performance. Within the silicon substrate [see Fig. 3(a)], the temperatures range from approximately 58 to 65°C, while the range in the nickel substrate is 57 to 68°C. The distances between 1°C temperature increments in the fin section of the nickel substrate are significantly smaller than those of the silicon substrate. However, the fin temperatures for both substrates are considerably higher than the bulk fluid temperature, thereby indicating high rates of heat transfer over the entire fin surfaces. The relative difference in overall thermal resistance $\mathscr{R}''$ between parts (a) and (b) of Fig. 3 is less than 10%.

3.2. Effects of channel width

Channel width has a significant effect on overall

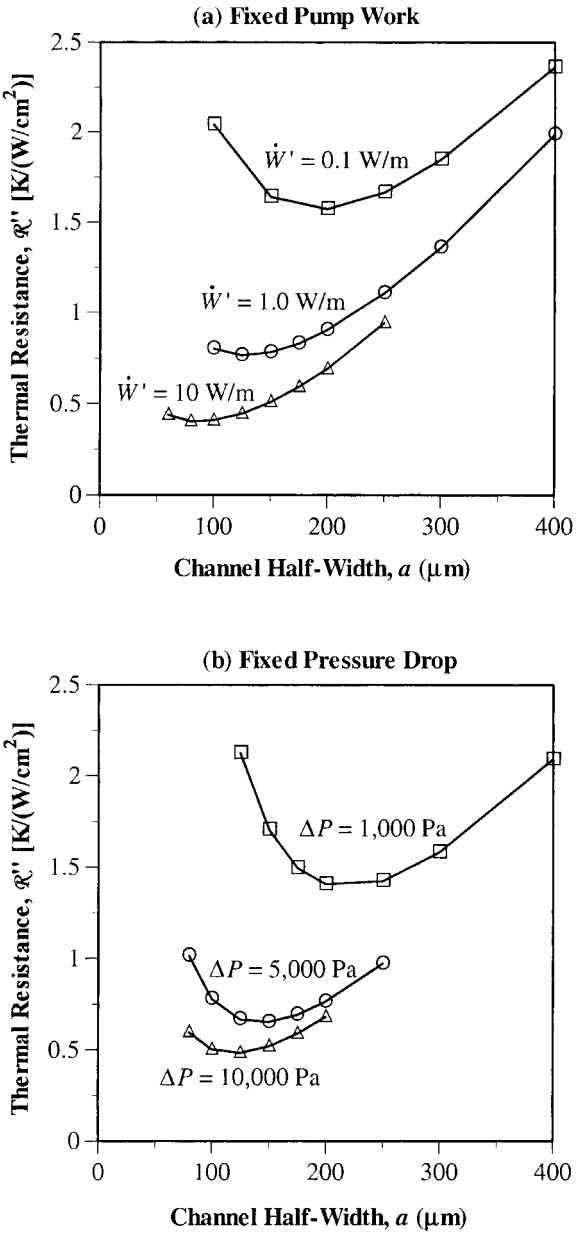

Fig. 4. Overall thermal resistance $\mathscr{R}''$ as function of channel half-width a. Fluid = water. Substrate = silicon. Fin half-thickness $t_f = 0.5a$. Channel height b = 1000 μm. Channel length L = 5 cm. Conduction thickness t_c = 500 μm. Curvature parameter $\epsilon = -0.12$. (a) Fixed pump work $\dot{W}'$. (b) Fixed pressure drop ΔP.

heat transfer due to the functional dependencies of the cross-sectional and bulk thermal resistances shown in Eqs. (40) and (43). Fig. 4 contains a graph of overall thermal resistance as a function of channel half-width for (a) fixed pump work and (b) fixed pressure drop. In both parts, the substrate is made of silicon, the fluid

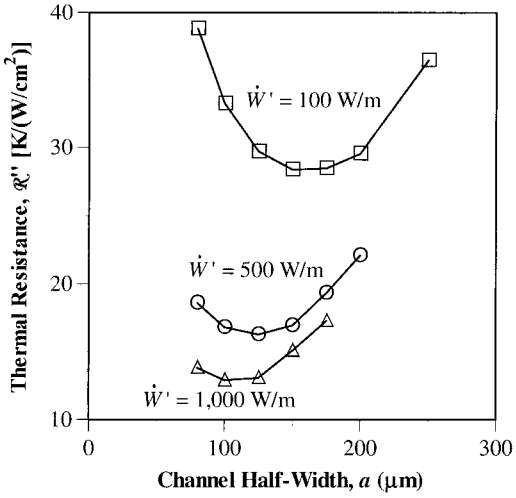

Fig. 5. Overall thermal resistance $\mathscr{R}''$ as function of channel half-width a and pump work $\dot{W}'$. Fluid = air. Substrate = silicon. Fin half-thickness $t_f = 0.5a$. Channel height b = 1000 μm. Channel length L = 5 cm. Conduction thickness t_c = 500 μm. Curvature parameter $\epsilon = -0.12$.

is water, the fin half-thickness is one-half the channel half-width, and the curvature parameter is $\epsilon = -0.12$.

Optimal channel half-widths in the range 75 μm $\leq a \leq$ 225 μm are evident for both parts of the figure. For small half-widths a, the total thermal resistance is dominated by the bulk resistance, which goes as a^{-1} and a^{-2} in Fig. 4(a) and Fig. 4(b), respectively. As the channel half-width increases, the cross-sectional resistance becomes more significant relative to bulk resistance, resulting in a minimum total resistance. The optimal half-width increases as the driving force (either pump work or pressure drop) decreases. The more pronounced minima for the fixed pressure drop constraint are caused by the a^{-2} dependence of bulk resistance compared to the a^{-1} dependence for the fixed pump work constraint.

The driving force (either pump work or pressure drop) necessary to produce sufficient cooling rates for high-power devices is seen to be quite reasonable. The results in Fig. 4 indicate that, for optimal geometries, heat fluxes greater than 100 W/cm^2 are achievable for a temperature rise of 50°C above the ambient for modest driving forces of either $\dot{W}' = 10$ W/m or ΔP = 10,000 Pa. Previous workers [1,4] have focused more attention on larger driving forces, for which developing or turbulent flow can produce lower resistances than fully developed, laminar flow. However, the thermal resistance levels shown in Fig. 4 are consistent with the projected cooling needs of high power electronic devices [34].

The thermal performance of air-cooled heat sinks is significantly worse than that of water-cooled heat

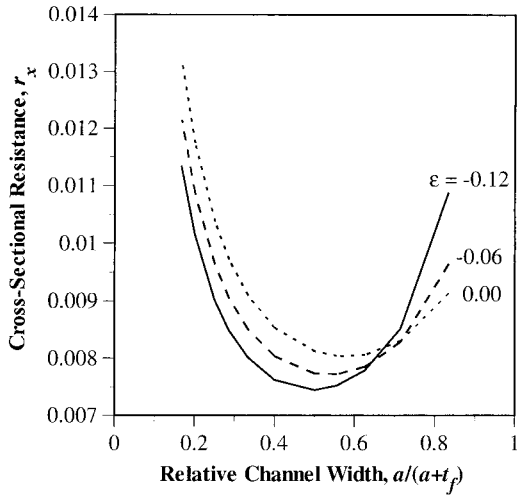

Fig. 6. Scaled, cross-sectional thermal resistance r_x as function of relative channel width $a/(a+t_f)$ and curvature parameter ϵ. Channel aspect ratio $\alpha^*=0.1$. Conductivity ratio $k_s/k_f=243$. Relative substrate height $(b+t_c)/b = 1.5$.

sinks. A graph of thermal resistance vs channel half-width is shown in Fig. 5, in which the fixed geometric parameters are identical to those in Fig. 4. Each curve in Fig. 5 represents a fixed value of pump work. Even though the input work rates are much higher than those in Fig. 4 for water, the resulting thermal resistances for air are much higher. To achieve significantly lower resistances, higher work rates and/or longer fins would be required. The resulting flow conditions would likely fall into the developing or turbulent regimes, as described, for instance, by Philips [4].

3.3. Effects of channel shape and fin thickness

We now focus attention on the effects of the curvature parameter ϵ and its relationship with the fin half-thickness t_f. The channel shape influences both the cross-sectional resistance $\mathscr{R}''_x$ (or r_x in nondimensional form) and the bulk resistance $\mathscr{R}''_{bulk}$.

For rectangular channels with high aspect ratios, Tuckerman [3] analyzed (and Weisberg et al. [5] confirmed via computations) that the minimum cross-sectional resistance occurs when the channel width relative to the channel period is $a/(a+t_f)=0.5$. However, this simple relationship may not be valid for fins of variable cross section. Fig. 6 illustrates the relationship between the cross-sectional resistance r_x and the relative channel width $a/(a+t_f)$ for several different values of the curvature parameter ϵ. For all curves, the channel aspect ratio is $\alpha^* \equiv 2a/b = 0.1$, and the thermal conductivity ratio is $k_s/k_f=243$.

The results in Fig. 6 confirm the minimum at $a/(a+t_f)=0.5$ for the rounded-rectangular boundary shape ($\epsilon=-0.12$). However, as the boundary becomes more curved with increasing ϵ, the minimum shifts toward larger relative channel widths. For the elliptical shape ($\epsilon=0.00$), the minimum occurs at a relative channel width of 0.58. This shift suggests that, with curved channel boundaries, a given substrate may con-

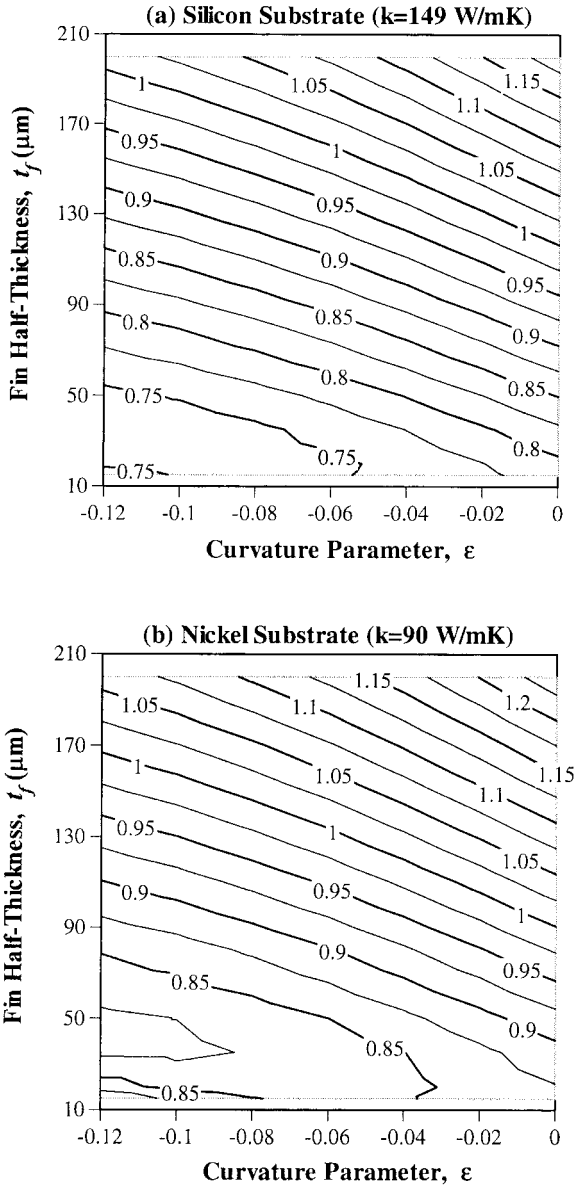

Fig. 7. Overall thermal resistance $\mathscr{R}''$ as function of fin half-width t_f and curvature parameter ϵ. Fixed pump work $\dot{W}'=1$ W/m. Fluid = water. Contour values represent thermal resistance. Channel half-width $a = 150$ μm. Channel height $b = 1000$ μm. Channel length $L = 5$ cm. Conduction thickness $t_c=500$ μm. (a) Silicon substrate. (b) Nickel substrate.

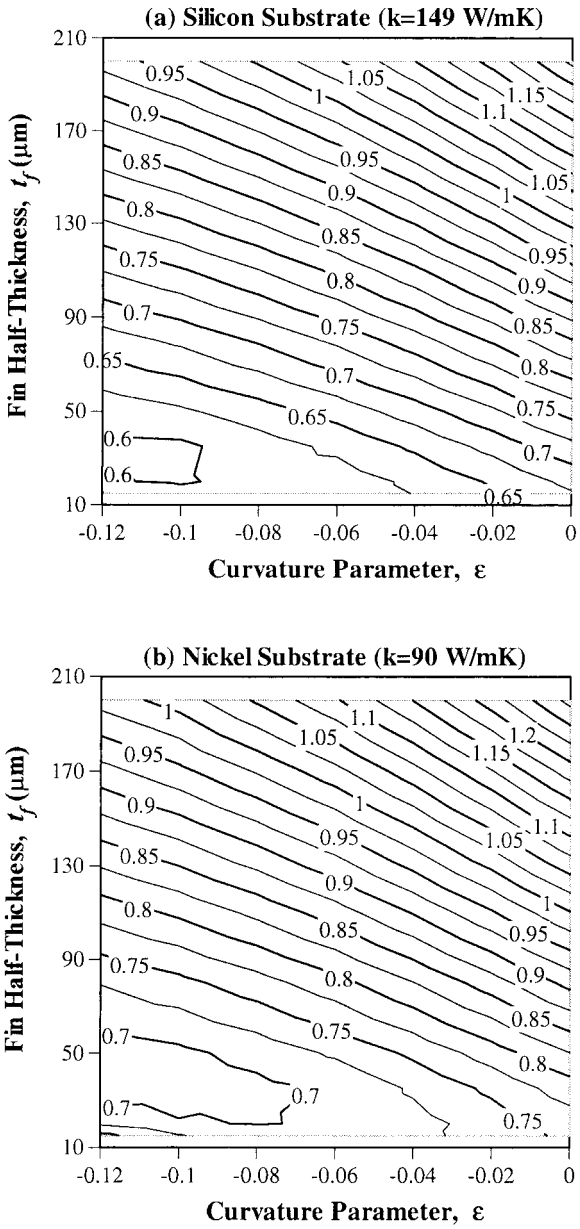

Fig. 8. Overall thermal resistance $\mathscr{R}''$ as function of fin half-width t_f and curvature parameter ϵ. Fixed pressure drop ΔP = 5000 Pa. Fluid = water. Contour values represent thermal resistance. Channel half-width a = 150 μm. Channel height b = 1000 μm. Channel length L = 5 cm. Conduction thickness t_c = 500 μm. (a) Silicon substrate. (b) Nickel substrate.

tain more channels and might therefore produce better overall thermal performance.

The relationship between channel curvature and fin thickness can be further illustrated by considering representative contour maps. Fig. 7 contains contours of overall thermal resistance as a function of channel curvature and fin thickness for a fixed pump work rate of $W' = 1$ W/m and a channel half-width of a = 150 μm, which is close to the optimum shown in Fig. 4. The coolant fluid is water.

Along the top left portion of the figure (i.e., for nearly rectangular channels with large fin thickness), the thermal resistance decreases with decreasing fin thickness because the density of coolant channels (and the associated convective surface area) increases. However, as the fin thickness decreases further, the fin efficiency decreases, resulting in an optimal fin thickness. The optimal fin thickness is smaller for the silicon substrate [Fig. 7(a)], due to its higher thermal conductivity, than for the nickel substrate [Fig. 7(b)].

Increasing the channel curvature decreases the optimal fin thickness for both substrates in Fig. 7. For a rounded-rectangular boundary ($\epsilon = -0.12$), the optimal fin half-thicknesses are approximately 35 and 45 μm for silicon and nickel, respectively. However, for $\epsilon = -0.06$, the corresponding optima are 15 and 25 μm. Further, for a given fin half-thickness, the overall thermal resistance tends to increase by 10 to 15% from rounded-rectangular channels ($\epsilon = -0.12$) to elliptical channels ($\epsilon = 0.00$). Although increased channel curvature tends to decrease thermal performance, the results in Fig. 7 indicate that the effect is small and should not be a major concern when using fabrication techniques that produce curved channel boundaries.

For fixed pressure drop, the relationship between curvature and fin thickness remains similar to that described above. Fig. 8 contains contours of overall thermal resistance as a function of channel curvature and fin thickness for a fixed pressure drop of ΔP = 5000 Pa. In this case, thermal resistance increases more rapidly with large, increasing fin thicknesses due to the linear relationship $\mathscr{R}''_{\text{bulk}} \sim t_f$ [see Eq. (43)] compared to the square-root dependence for fixed pump work. Similarly, increased channel curvature (which increases the mean fin thickness) causes a slightly larger decrease in thermal performance for a given fin thickness. In the optimal region, increased channel curvature again significantly decreases the optimal fin half-thickness. The contour maps included here should allow designers to better understand the effects of channel curvature, which is sometimes unavoidable, and fin thickness on overall thermal performance.

4. Summary and conclusions

Conjugate heat conduction and convection have been studied for fully developed flow in substrates with embedded channels with curved cross-sectional boundaries. The complex variable boundary element method

provides a relatively straightforward and accurate means of analysis for channel cross sections with high curvature and high aspect ratios. The computational method is well-suited for the problems considered here because the whole-domain boundary integrals (both singular and non-singular) are evaluated exactly and are path independent. However, Neumann boundary condition integrals over a boundary segment require numerical quadrature.

The results indicate that, as compared to rectangular channels, curved boundaries can reduce the optimal fin thickness (see Fig. 6), thereby reducing the separation between channels. In general, the overall thermal resistance produced by a curved channel boundary is slightly higher than that of a rectangular channel with an equal fin-tip thickness (see Figs. 7 and 8). However, when optimized, the two types produce virtually the same thermal resistance. The computational method employed here could be extended to other thermal problems for which the accurate modeling of curved boundaries is necessary.

Acknowledgements

The authors thank Prof. S. Mukherjee for helpful conversations. The research was funded by the Industry–Cornell University Alliance for Electronic Packaging, with corporate support from AMP, IBM, and 3 M. TSF was supported by a graduate fellowship from the Semiconductor Research Corporation.

References

[1] D.B. Tuckerman, R.F.W. Pease, High performance heat sinking for VLSI, IEEE Electron Device Letters 2 (5) (1981) 126–129.
[2] D.B. Tuckerman, R.F.W. Pease, Optimized convective cooling using micromachined structures, Journal of the Electrochemical Society 129 (3) (1982) C98.
[3] D.B. Tuckerman, Heat-transfer microstructures for integrated circuits, Ph.D. thesis, Stanford University, 1984.
[4] R.J. Philips, Microchannel heat sinks., in: A. Bar-Cohen, A.D. Kraus (Eds.), Advances in Thermal Modeling of Electronic Components and Systems, vol. 2, ASME Press, New York, 1990, Chapter 3.
[5] A. Weisberg, H.H. Bau, J.N. Zemel, Analysis of microchannels for integrated cooling, International Journal of Heat and Mass Transfer 35 (10) (1992) 2465–2473.
[6] X. Yin, H.H. Bau, Uniform channel micro heat exchangers, ASME Journal of Electronic Packaging 119 (2) (1997) 89–94.
[7] T.L. Hoopman, Microchanneled structures, in: D. Cho, R. Warrington, C. Blechinger, A. Pisano, W. Trimmer, L. Trefethan (Eds.), Microstructures, Sensors, and Actuators, vol. 19, ASME DSC, 1990, pp. 171–174.
[8] R.W. Knight, D.J. Hall, J.S. Goodling, R.C. Jaeger, Heat sink optimization with application to microchannels, IEEE Transactions on Components, Packaging, and Manufacturing Technology 15 (5) (1992) 832–842.
[9] M.B. Kleiner, S.A. Kuhn, K. Haberger, High performance forced air cooling scheme employing microchannel heat exchangers, IEEE Transactions on Components, Packaging, and Manufacturing Technology—Part A 18 (4) (1995) 795–804.
[10] S.M. Marco, L.S. Han, A note on limiting laminar Nusselt number in ducts with constant temperature gradient by analogy to thin-plate theory, Transactions of the ASME 77 (1955) 625–630.
[11] S. Timoshenko, S. Woinowsky-Krieger, Theory of Plates and Shells, McGraw-Hill, New York, 1959.
[12] L. Gu, M-K. Huang, A complex variable boundary element method for solving plane and plate problems of elasticity, Engineering Analysis with Boundary Elements 8 (6) (1991) 266–272.
[13] I.N. Vekua, New Methods for Solving Elliptic Equations, Wiley and Sons, New York, 1967.
[14] F.A.A. Barbuto, R.M. Cotta, Integral transformations of elliptic problems within irregular domains, International Journal for Numerical Methods for Heat and Fluid Flow 7 (8) (1997) 778–793.
[15] R.M. Cotta, Integral Transforms in Computational Heat and Fluid Flow, CRC Press, Boca Raton, FL, 1993.
[16] T.V. Hromadka, G.L. Guymon, Application of a boundary integral equation to prediction of freezing fronts in soils, Cold Regions Science and Technology 6 (2) (1982) 115–121.
[17] P. Brevig, M. Greenhow, T. Vinje, Extreme wave forces on submerged wave energy devices, Applied Ocean Research 4 (4) (1982) 219–225.
[18] T.V. Hromadka, The Complex Variable Boundary Element Method, Springer-Verlag, New York, 1987.
[19] T.V. Hromadka, C. Lai, The Complex Variable Boundary Element Method in Engineering Analysis, Springer-Verlag, New York, 1987.
[20] J.H. Choi, B.M. Kwak, A boundary integral equation formulation in derivative unknowns for two-dimensional potential problems, Journal of Applied Mechanics 56 (1989) 617–623.
[21] R. Kolhe, W. Ye, C-Y. Hui, S. Mukherjee, Complex variable formulations for usual and hypersingular integral equations for potential problems—with applications to corners and cracks, Computational Mechanics 23 (5) (1996) 279–286.
[22] D. Homentcovschi, L. Kreindler, The CVBEM based on a cubic spline trial function, Engineering Analysis 5 (3) (1988) 161–165.
[23] R.T. Bailey, C.K. Hsieh, A quadratic-element formulation of the complex variable boundary element method, International Journal for Numerical Methods in Fluids 15 (1992) 841–863.
[24] K.J. Lee, A boundary element method for plane isotropic elastic media using complex variable technique, Computational Mechanics 11 (1993) 83–91.
[25] R.T. Bailey, C.K. Hsieh, H. Li, Grid generation in two dimensions using the complex variable boundary el-

ement method, Applied Mathematical Modeling 19 (1995) 322–332.
[26] T.V. Hromadka, Modeling error in evaluation of the CVBEM matrix system, Engineering Analysis with Boundary Elements 17 (1996) 85–90.
[27] T.V. Hromadka, Determining relative error bounds for the CVBEM, Engineering Analysis 2 (2) (1985) 75–80.
[28] T.V. Hromadka, Locating CVBEM collocation points for steady state heat transfer problems, Engineering Analysis 2 (2) (1985) 100–106.
[29] T.S. Fisher, Optimal free- and forced-convection cooling of electronics, Ph.D. thesis, Cornell University, 1998.
[30] T.S. Fisher, K.E. Torrance, Analysis of fully developed heat transfer in ducts of general, curved cross section by the complex variable boundary element method, International Journal for Numerical Methods in Engineering 45 (12) (1999) (in press).
[31] G.F. Carrier, M. Krook, C.E. Pearson, Functions of a Complex Variable, Hod Books, Ithaca, NY, 1983.
[32] M.D. Greenberg, Foundations of Applied Mathematics, Prentice-Hall, Englewood Cliffs, NJ, 1978.
[33] X. Wei, A. Chandra, L-J. Leu, S. Mukherjee, Shape optimization in elasticity and elasto-viscoplasticity by the boundary element method, International Journal of Solids and Structures 31 (4) (1994) 533–550.
[34] SEMATECH, The National Technology Roadmap for Semiconductors: Technology Needs, SEMATECH, Austin TX,1997.